Supplementary Information (SI) for Energy & Environmental Science.
This journal is © The Royal Society of Chemistry 2026

Supporting Information

Lattice Reconstruction Strategy for Fast-Charging Plateau-Type Hard Carbon Anode in Ultra-Long-Life Sodium-Ion Batteries

Feng Wang,[a]# Lian Chen,[a,b]# Fan Li,[b] Yongben Zheng,[b] Jiaqi Wei,[c] Caozheng Diao,[d] Ihor Radchenko,[e] Jie Shi,[a] Linwei Li,[b] Jingshu Wang,[b] Zhengshuai Bai,[b] Yanyan Zhang,[b] Oleksandr I. Malyi,*[a,e] Xiaodong Chen,[c] Yuxin Tang,*[a,b]

[a] Qingyuan Innovation Laboratory, 1 Xueyuan Road, Quanzhou 362801, P. R. China

[b] College of Chemical Engineering, Fuzhou University, Fuzhou 350116, P. R. China

[c] Innovative Centre for Flexible Devices (iFLEX), School of Materials Science and Engineering, Nanyang Technological University, 50 Nanyang Avenue, Singapore, 639798 Singapore

[d] Singapore Synchrotron Light Source, National University of Singapore, 5 Research Link, Singapore, 117603 Singapore

[e] Centre of Excellence ENSEMBLE^3 Sp. z o. o., Wolczynska Str. 133, 01-919, Warsaw, Poland

#These two authors contribute equally to this work.

Corresponding authors:

E-mail: oleksandrmalyi@gmail.com; yxtang@fzu.edu.cn

Experimental Section

Preparation of the hard carbon anode

The hard carbon was synthesized following a modified two-stage protocol based on a previous report[1]. The first stage, referred to as the defect optimization step, was performed at a selected temperature (T_1= 500, 800, 1100, or 1300 °C) under argon to modulate oxygen functionalities and defect density, aiming to suppress parasitic electrolyte reactions while preserving beneficial redox-active groups. The second stage, the lattice reconstruction step, was uniformly conducted at 1500 °C to promote a disordered carbon structure with enlarged interlayer spacing and reduced graphitic crystallite size, which is critical for achieving a pronounced low-voltage plateau in sodium storage. Specifically, bamboo-derived hard carbon labeled HC800 was first heated to 800 °C at 5 °C/min and held for 150 min, followed by carbonization at 1500 °C (5 °C/min, 30 min) under argon. Analogously, the HC500, HC1100, and HC1300 samples were prepared by varying T_1 while keeping the second stage identical. For comparison, conventional single-stage hard carbons were prepared by direct carbonization at 1300 °C or 1500 °C for 180 min (5 °C/min), denoted as HC1300-180 and HC1500-180, respectively. Additionally, to further tailor surface chemistry, a pre-oxidation step was introduced by heating the precursor in air at 300 °C (5 °C/min, 120 min) prior to the synthesis of all samples, which helps eliminate unstable oxygen groups and generate additional reversible sodium ion storage sites.

Electrochemical measurement

The electrochemical performance of all electrodes was examined using coin-type (type CR2032) cells with sodium foil as a counter. All hard carbon electrode materials were prepared by mixing of active material, sodium carboxymethyl cellulose, and Super P, and (90:5:5) onto a copper foil current collector which has an average mass load of approximately 2.0-3.0 mg cm^{-2} without gas protection; 1 M $NaPF_6$ in glyme (DME) was used as the electrolyte and a glass fiber film (Whatman GF/A) was used as the separator. The O3-type $NaNi_{1/3}Fe_{1/3}Mn_{1/3}O_2$ layered oxide material was used in full cell evaluation, and prepared by mixing active material, PVDF, and Super P (95:3:2) onto an Al foil current collector, which has an average mass load of approximately 10 mg cm^{-2}. The pouch cells were further constructed using the HC800 as anode and O3-type $NaNi_{1/3}Fe_{1/3}Mn_{1/3}O_2$ layered oxide materials as cathode. The capacity ratio of anode to cathode was ~1.1, and the mass loading of anode was ~10 mg cm^{-2}. Galvanostatic charge and discharge measurements at different current densities and galvanostatic intermittent titration technique (GITT) were carried out on a battery controlling system (NEWARE Battery Testing System, CT-4008Tn-5V50mA-HWX) in a voltage range from 2.0 to 0.005 V (versus Na/Na^+). Cyclic voltammetry (CV) and Electrochemical impedance spectroscopy (EIS) measurements were carried out by a cell test system (Par-solartron 1400). All the electrochemical measurements above were conducted at 25 °C. The overall GITT profile of hard carbon electrodes during charge and discharge with a pulse current at 50 mA g^{-1} for 10 min between rest intervals for 120 minutes. Use the following equation to calculate $D_{Na}{}^+$:

$$D_{Na} = \frac{4}{\pi t}\left(\frac{mV}{MS}\right)^2\left(\frac{\Delta E_s}{\Delta E_t}\right)^2 \ (t << \frac{l^2}{D_{Na}}) \qquad \text{S1}$$

where τ stands for the period of the current pulse at a specific current density; m, M, V, S, and l represent the mass loading, the molecular weight, the molar volume, the electrode effective contact area, and the thickness, respectively.

Materials characterization

X-ray diffraction (XRD, Rigaku D/Max 2500, Japan) was conducted to study the crystal structure and phase composition. Raman spectra were collected from a Raman spectrometer (Jobin Yvon, HR800) with a 532 nm laser beam. X-ray photoelectron spectra (XPS) were performed on a KRATOS Axis Ultra-X-ray photoelectron spectrometer with a monochromatized Al Kα radiation at 225 W. N_2 adsorption-desorption was performed using the BELSORP MAX analyzer. The pycnometry experiments of the prepared hard carbons were conducted on BELPycno (MicrotracBEL Japan, Inc.) to detect the skeletal density. True density was determined by helium pycnometry. Closed-pore characteristics were evaluated by small-angle X-ray scattering (SAXS) on a Rigaku NANOPIX 3.5 m system equipped with a Cu Kα source. The TOF-SIMS measurements were conducted using a TOF-SIMS IV (ION-TOF GmbH, Germany) with a bismuth liquid metal ion source (25 keV). The analysis area was 200 × 200 μm^2. Depth profiles were obtained by sputtering with a Cs^+ ion beam (1 keV). The composition of the SEI was investigated by XPS, Thermo Scientific K-Alpha with depth profiling on

HC electrodes after 50 cycles at 50 mA g^{-1}. Note that the denoted etching depth was roughly calculated based on the Ar^+ etching time. In-situ EIS for three electrode HC cells were performed using Solartron Metrology at 25 °C.

DRT and DCT analysis

The distribution of relaxation times (DRT) and the distribution of capacitive times (DCT) were used to unravel various processes in the hard carbon. DRT and DCT deconvolution used the impedance and admittance data, respectively. DRT impedance, $Z_{DRT}(f)$, at a frequency f, can be expressed as[2]

$$Z_{DRT}(f) = i2\pi f L_0 + R\infty + \int_{-\infty}^{+\infty} \frac{\gamma(log\tau)}{1 + i2\pi f\,\tau} dlog\,\tau \qquad \text{S2}$$

where L_0, $R\infty$, τ, and $\gamma(log\tau)$ are an inductance, an ohmic resistance, a timescale, and the DRT, respectively. In turn, the total polarization resistance, R_{pol}, was computed using the following integral:

$$Rpol = \int_{-\infty}^{+\infty} \gamma(log\tau) dlog\,\tau \qquad \text{S3}$$

The DRT analysis was conducted as reported previously[3] with a regularization parameter of 0.001. The DCT admittance, $Y_{DCT}(f)$, at a frequency f, is given by[4]

$$Y_{DCT}(f) = i2\pi f C_0 + G\infty + i2\pi f \int_{-\infty}^{+\infty} \frac{\gamma_{DCT}(log\tau)}{1 + i2\pi f\,\tau} dlog\,\tau \qquad \text{S4}$$

where C_0, $G\infty$, and $\gamma_{DCT}(log\,\tau)$ are capacitance, ohmic conductance, and DCT, respectively.

The total conductance, $G_{S,tot}$, is given by:

$$G_{S,tot} = f \int_{-\infty}^{+\infty} \gamma_{DCT}(log\,\tau)\, dlog\,\tau \qquad \text{S5}$$

In-situ Raman and *in-situ* XRD for hard carbon

The hard carbon electrodes were prepared with 90 wt.% active materials and 10 wt.% polytetrafluoroethylene (PTFE) with a mass loading of 10 mg cm^{-2}. A thin quartz window with a thickness of 0.5 mm was fixed on the top of the *in-situ* Raman cells, through which the signals were collected. An *in-situ* cell was tested by a beryllium window for XRD. The *in-situ* cells were tested in the potential range of 0.005-2 V at a constant current density of 50 mA g^{-1}.

Numerical calculations

To describe the charge/discharge process of hard carbon electrode and specifically capture Na concentration (C) as a function of time (t) and coordinate (x), we employ a numerical solution for Fick's second law, assuming isotropic Na diffusion (D) in the system within a one-dimensional model:

$$\frac{\partial C}{\partial t} = D\frac{\partial^2 C}{\partial x^2} \tag{S6}$$

To solve eq.1, the finite difference method is directly implemented as

$$\frac{\partial C}{\partial t} \approx \frac{C_i^{n+1} - C_i^n}{\Delta t}, \frac{\partial^2 C}{\partial x^2} \approx \frac{C_{i+1}^n - 2C_i^n + C_{i-1}^n}{\Delta x^2} \tag{S7}$$

$$C_i^{n+1} = C_i^n + \frac{D\Delta t}{\Delta x^2}(C_{i+1}^n - 2C_i^n + C_{i-1}^n) \tag{S8}$$

where C_i^n, C_{i+1}^n, and C_{i-1}^n represent the concentrations at positions i, i+1, and i-1 at the nth time step, respectively. According to Fourier stability analysis, $D\Delta t/(\Delta x^2)$ should be less than or equal to 0.5. Using the iterative formula, one can obtain the concentration distribution at the next time step from that at the previous time step, thereby constructing C(x, t). In the initial state of diffusion (t=0), the sodium-ion concentration in the hard carbon, C_0, is zero, while the concentration at the electrolyte–electrode interface, C_{max}. By this method, one obtains the Na-ion concentration profile in hard carbon, C(x,t), from which both the relative capacity (Eq. S9) and the Degree of Charge (DOC, Eq. S10) can be computed as

$$Capacity = \int_0^L C(x,t)dx \tag{S9}$$

$$DOC(t) = \frac{Current\ Na\ intercalation\ amount}{Maximum\ Na\ intercalation\ capacity} \times 100\% \tag{S10}$$

First-principles calculations

For all first-principles calculations, we used the density-functional theory (DFT) with the projector augmented wave (PAW) method[5] as implemented in the Vienna Ab-initio Simulation Package (VASP)[6-8]. The energy cutoff was set to 500 eV for the plane-wave basis set. The position and lattice optimization were performed until the forces were less than 0.01 eV/Å. Brillouin zones were sampled using a Γ-centered k-point mesh corresponding to 10,000 k-points per reciprocal atom. Since graphite (a representative local motif in hard carbon) is a van der Waals (vdW) bonded material, all calculations are given for optB88-vdW[9] that allows for an accurate description of vdW interaction in the graphite system. Na diffusion has been studied using the nudged elastic bands method (NEB)[10, 11], as implemented in VASP.

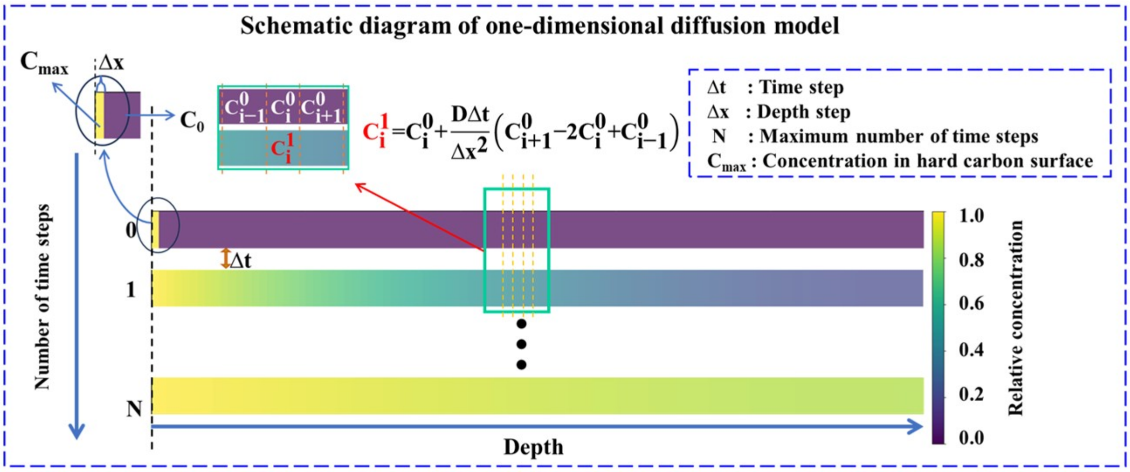

Figure S1. The finite-element diffusion model for one-dimensional diffusion.

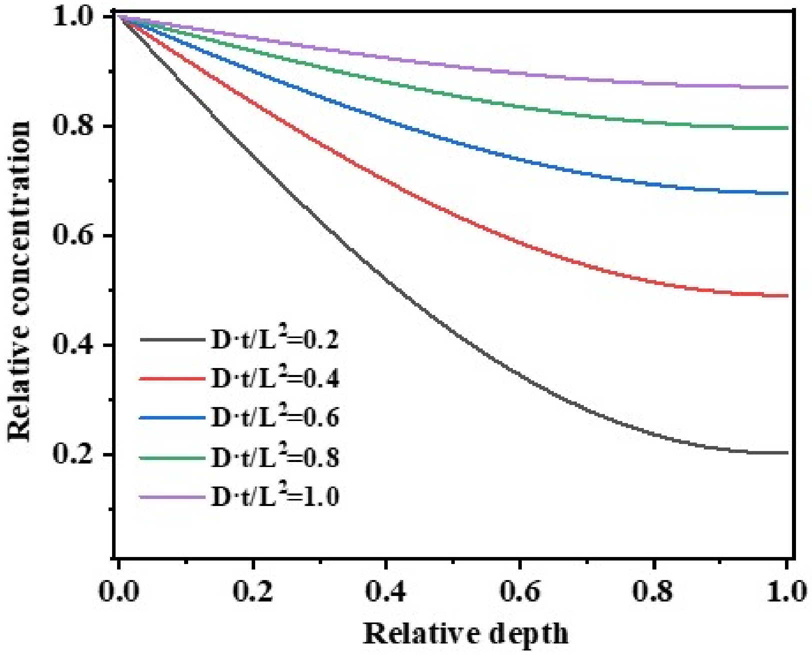

Figure S2. The data for concentration distribution as a function of x point for the same diffusivity but at different moments of time.

Text: To study Na intercalation into hard carbon, we limited ourselves to a single structural motif in the hard carbon - the graphite-like system with different distances between the carbon layers. To study the effect of the interlayer distance, we used an expanded graphite model with AB layer stacking ($P6_3/mmc$) with different distances between the carbon layers. In the intercalation calculations, we always used 6×6×2 graphite supercells based on the $P6_3/mmc$ C structure retrieved from the Materials Project after performing structural optimization with the optB88-vdW functional. To get the increased interlayer spacing, we (1) strained the supercells along the **c** direction (across the carbon layers); (2) fixed the C atom motion along the **c** direction so that the interlayer spacing could not change. We estimated the voltage V_s for a single Na atom as follows.[12]

$$V_s = -\left(E_{Na+C} - E_C - E_{Na}\right)/e$$

here, e, E_{Na+C}, E_C, and E_{Na} are the Na charge, the total energies of single Na in expanded graphite, pristine expanded graphite, and metallic Na, correspondingly. The reference energy of metallic Na was calculated for $Im\bar{3}m$ Na structure from Materials Project[13].

To study Na diffusion and Na intercalation voltage, we first found the lowest-energy Na position inside AB graphite. We sampled Na positions within the graphite supercell, scanning the coordinate grid with 0.1 Å step. Then, we excluded all the Na positions that are (1) very close to any carbon atom (distance between the Na and C shorter than $0.5 \times$ sum of the Na and C ionic radii); or (2) very close to other considered Na positions; or (3) symmetrically equivalent with other Na positions. For each Na position, we performed structural relaxation, and then selected the lowest-energy Na-graphite configuration for each interlayer distance. Some relaxed Na configurations did not keep the original AB graphite stacking. Taking into account the focus of this model, we did not consider such configurations in our investigation, as they represent a different possible structural motif. The obtained lowest-energy configurations are summarized in **Figure S3, ESI†**.

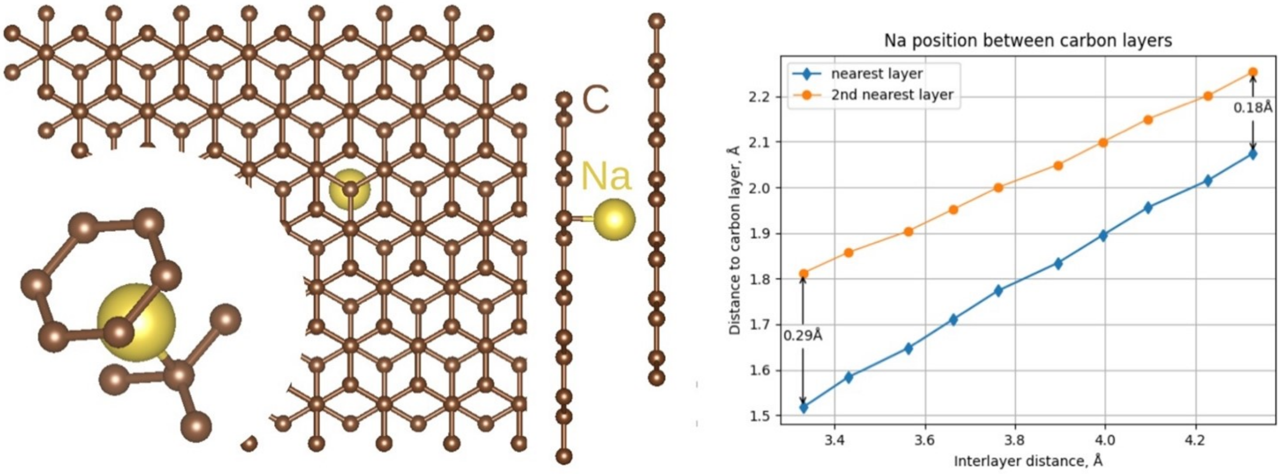

Figure S3. Lowest-energy Na position inside AB graphite-like motif of hard carbon with various interlayer distances. **(left)** The Na is not located precisely in the middle between layers - it is slightly closer to the center of the carbon ring. **(right)** As the interlayer distance increases, the Na position moves towards the middle point between the carbon layers.

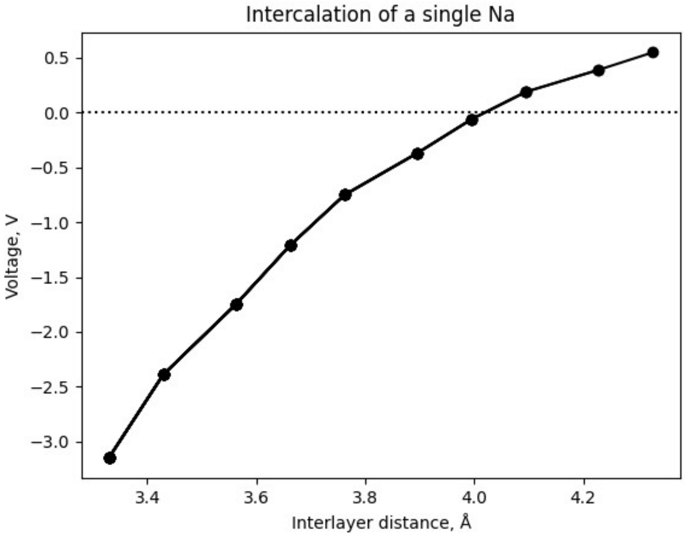

Figure S4. Voltage for a single Na inserted into AB graphite-like structural motif of hard carbon with varying interlayer distance. The voltage is negative when the interlayer distance is small (close to the equilibrium graphite distance), but becomes positive when the distance increases above 4 Å.

The calculated sodiation voltage is shown in **Figure S4, ESI†**. The voltage is negative for small interlayer distances (close to equilibrium graphite spacing) – Na intercalation is not energetically favorable. However, as the interlayer distance increases, the sodiation voltage monotonically increases. Above 4 Å, the voltage becomes positive, indicating that Na intercalation in hard carbon becomes possible when its d-spacing is sufficiently large.

To study Na diffusion inside expanded graphite, we performed NEB calculations. The initial guess for NEB calculations was produced by linear interpolation between the initial and final Na^+ expanded graphite structures, with 5 intermediate NEB images. Some NEB calculation results were further refined by running an additional NEB calculation between converged NEB images (e.g., **Figure 1d**, diffusion along the carbon layers). For each NEB calculation, we considered a diffusion path between two symmetrically equivalent lowest-energy Na sites. The full list of the lowest-energy Na sites was obtained by applying all the space group operations corresponding to the pristine expanded graphite supercell. We then considered only a single shortest diffusion path along the carbon layers and a single shortest diffusion path across the carbon layers. All the longer diffusion paths we tested always converged to a sequence of these two base paths. In the NEB calculations, in addition to constraining carbon atoms to move along the **c**-axis, we fully fixed all the carbon atoms further than 8 Å from the Na. This was done to keep AB stacking in the carbon layers and avoid deviations from the structural motif we are interested in. The 8 Å was chosen as the largest distance to fix at least a single carbon atom in each carbon layer in the supercell without affecting the carbon atoms directly interacting with the diffusing Na.

The calculated diffusion barriers for Na diffusion in expanded graphite are summarized in **Figure 1d**. The Na diffusion is highly anisotropic – diffusion along the carbon layers has 2 orders of magnitude lower diffusion barrier compared to the diffusion through/across the carbon layers. As the interlayer distance increases from equilibrium graphite spacing (3.33 Å) up to what is observed experimentally for hard carbons (3.7-4.2 Å [14]), the diffusion barrier along the layers drops from 0.38 eV (for 3.33 Å d-spacing) down to 0.06 eV (4.33 Å) while the diffusion through the carbon layer becomes more complex (16.58 eV for 3.33 Å d-spacing vs. 20.43 eV for 4.33 Å). Our data on sodiation voltage and diffusion barriers in the expanded graphite indicate that the storage mechanism (intercalation) and charging kinetics can be strongly affected by hard carbon synthesis conditions. When the d-spacing is too small, intercalation could be suppressed, making other sodium storage mechanisms dominate. In contrast, if the d-spacing crosses some threshold, intercalation might become possible, and the Na diffusion becomes faster.

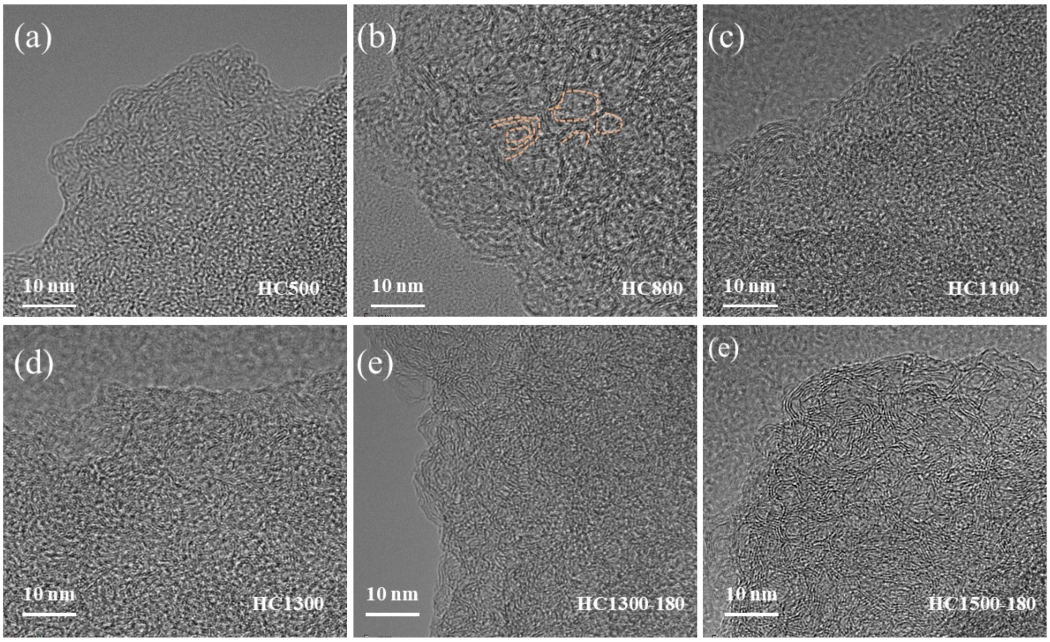

Figure S5. HRTEM images of the HC500, HC800, HC1100, HC1300, HC1300-180, and HC1500-180 samples.

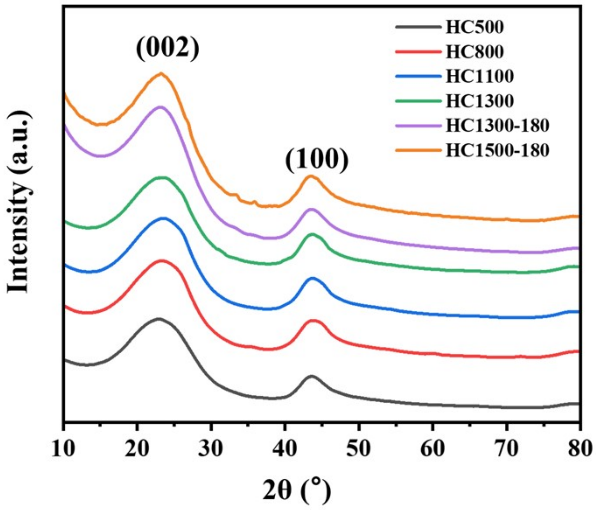

Figure S6. X-ray diffraction (XRD) patterns of the HC500, HC800, HC1100, HC1300, HC1300-180, and HC1500-180 samples.

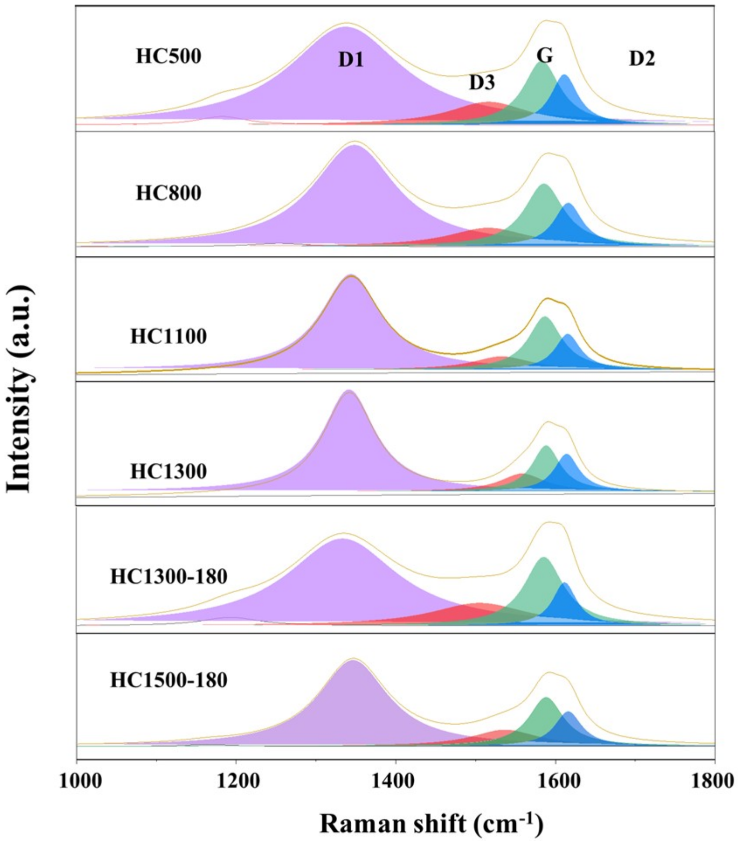

Figure S7. Raman spectra of the HC500, HC800, HC1100, HC1300, HC1300-180, and HC1500-180 samples.

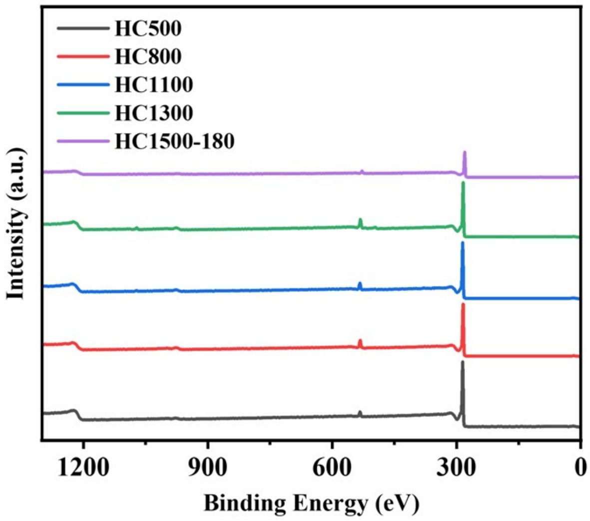

Figure S8. Wide-range X-ray photoelectron spectroscopy (XPS) spectra comparison of the HC500, HC800, HC1100, HC1300, and HC1500-180 samples.

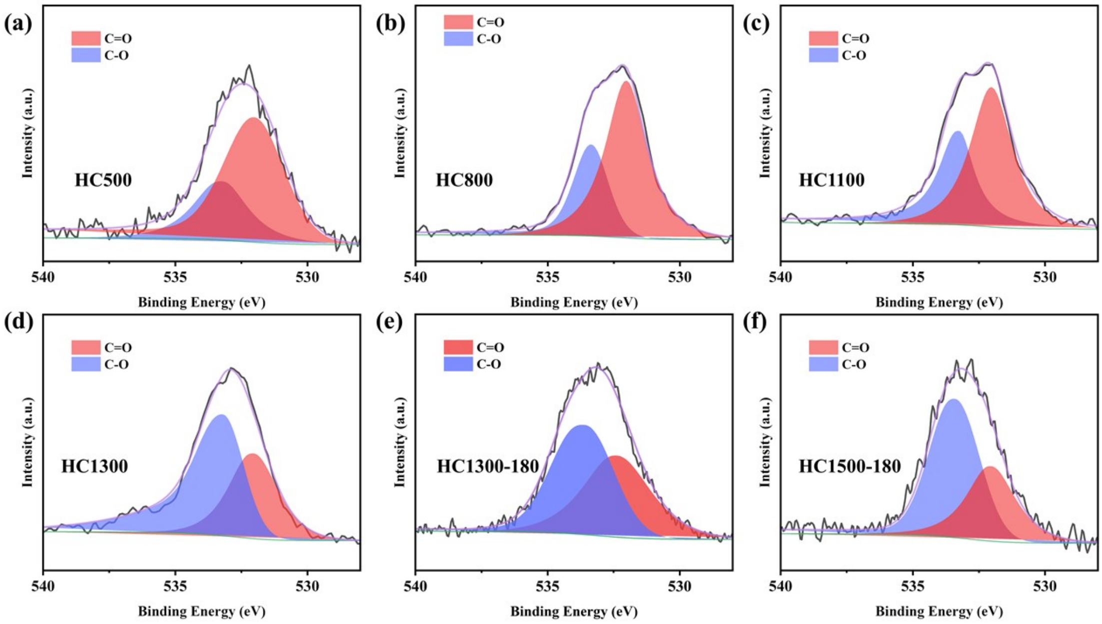

Figure S9. X-ray photoelectron spectroscopy (XPS) of O1s spectra comparison of the HC500, HC800, HC1100, HC1300, HC1300-180, and HC1500-180 samples.

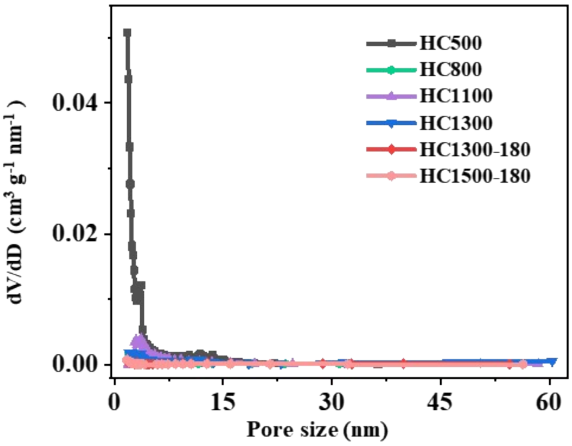

Figure S10. Pore size distribution obtained from the HC500, HC800, HC1100, HC1300, HC1300-180, and HC1500-180 samples.

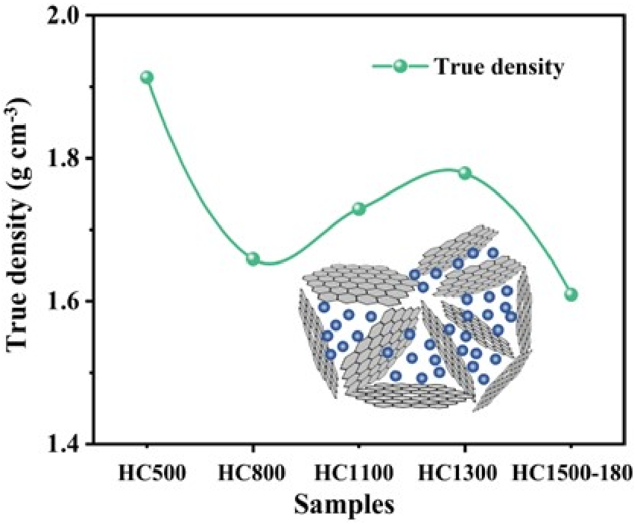

Figure S11. True density of the HC500, HC800, HC1100, HC1300, and HC1500-180 samples.

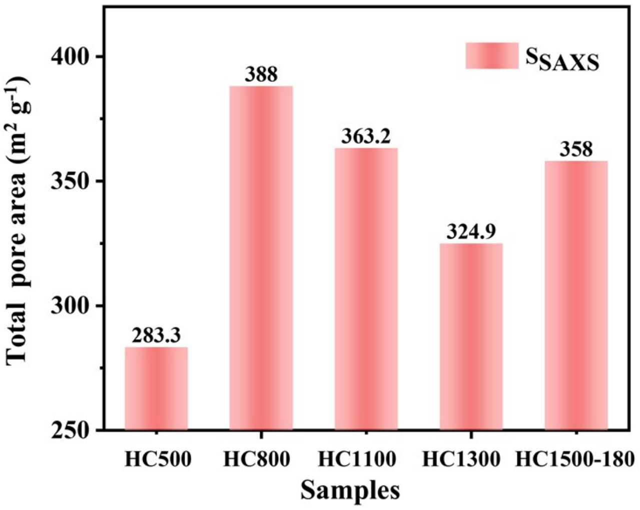

Figure S12. Total pore area of the HC500, HC800, HC1100, HC1300, and HC1500-180 samples.

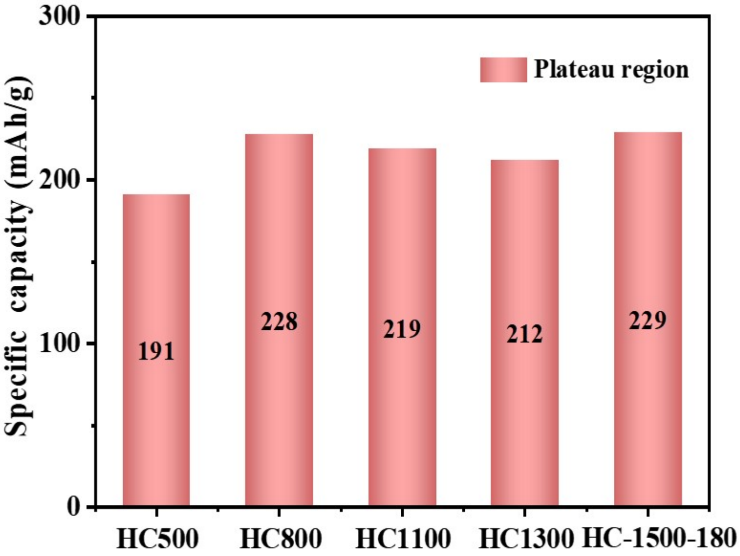

Figure S13. The plateau capacities in charge curves of the HC500, HC800, HC1100, HC1300, and HC1500-180 at 0.05 A g^{-1}.

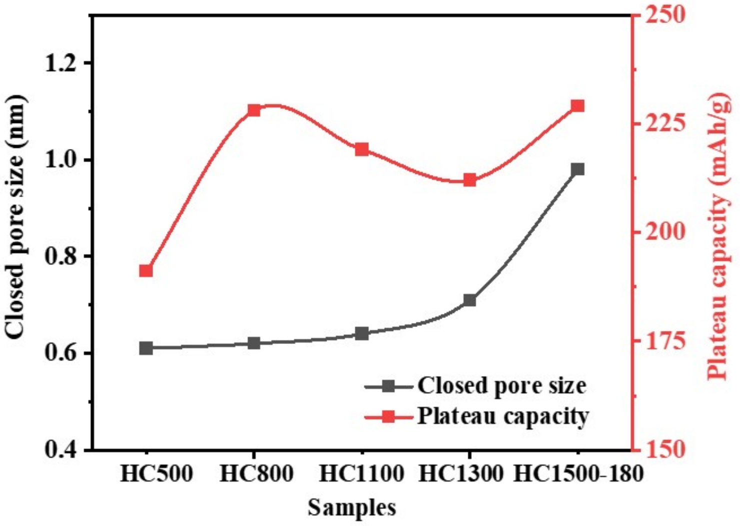

Figure S14. Correlation between closed pore size and plateau capacity of HC500, HC800, HC1100, HC1300, and HC1500-180 samples at 0.05 A g^{-1}.

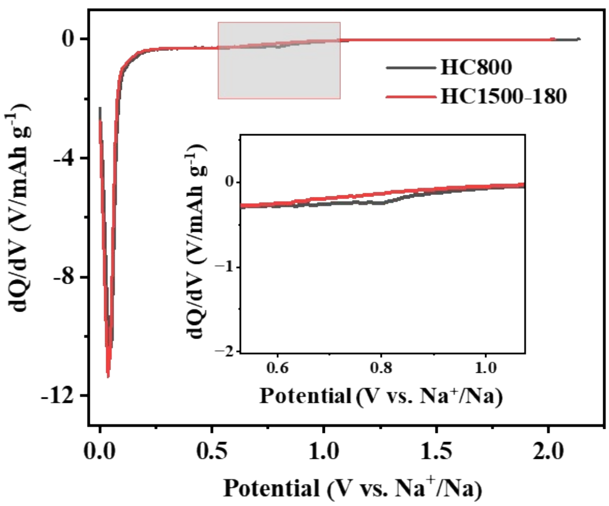

Figure S15. dQ/dV curves of HC800 and HC1500-180 at a current density of 0.05 A g^{-1} from 0.005 to 2.0 V.

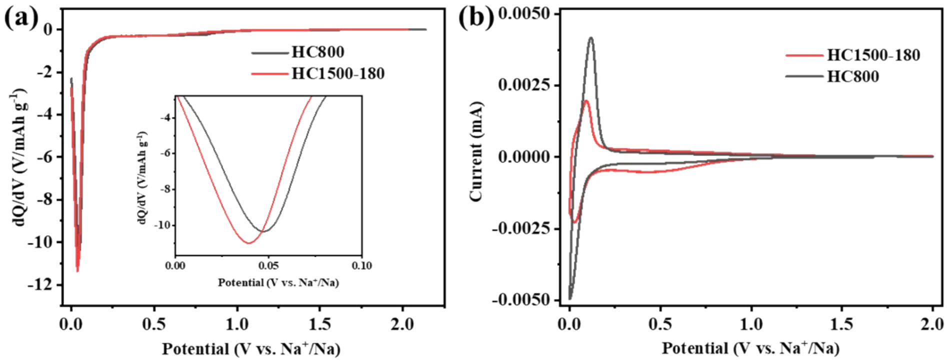

Figure S16. (a) dQ/dV curves of HC800 and HC1500-180 at 0.05 A g^{-1} from 0.005 to 2.0 V. (b) CV curves at a scan rate of 0.2 mV/s of HC800 and HC1500-180 in the first cycle.

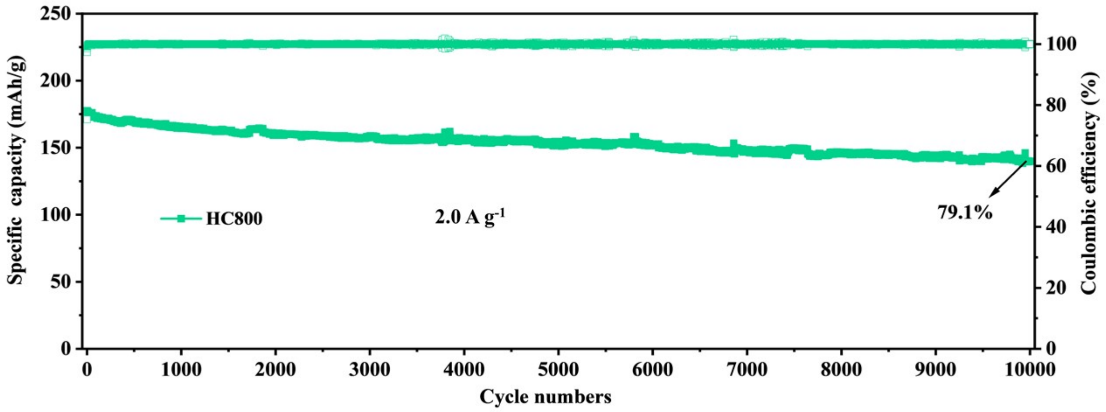

Figure S17. The HC800 of long-term cycling performance at high current density of 2.0 A g^{-1}.

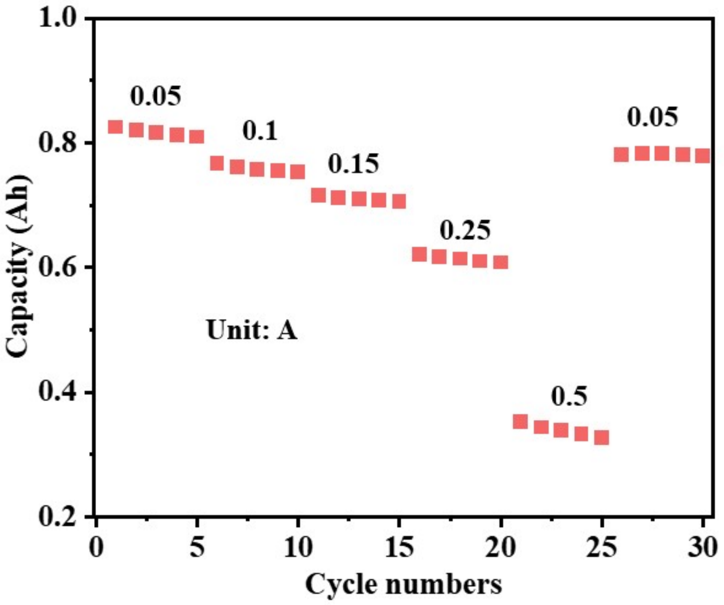

Figure S18. The rate performance of the $NaNi_{1/3}Fe_{1/3}Mn_{1/3}O_2$//HC800 pouch cell at different current densities.

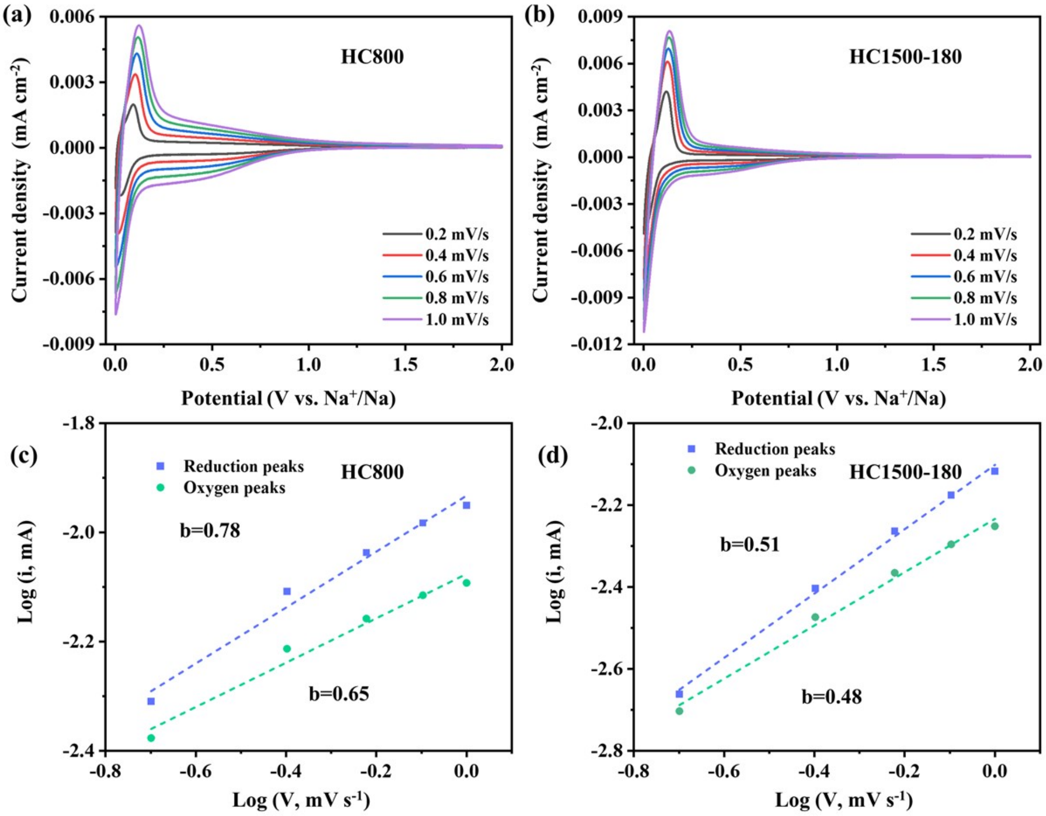

Figure S19. (a) CV curves at different scan rates and (c) linear relationship between peak currents of HC800 electrode. (b) CV curves at different scan rates and (d) linear relationship between peak currents of HC1500-180 electrode.

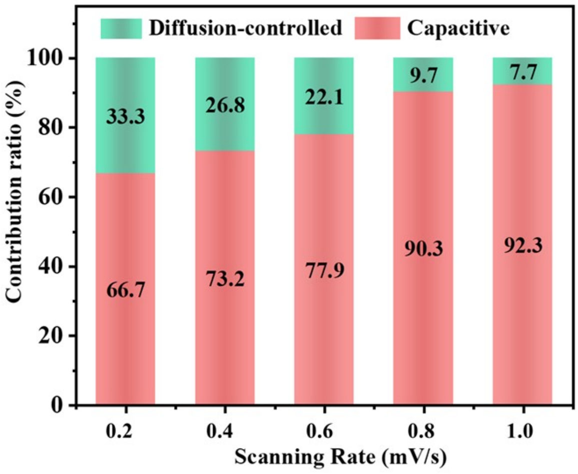

Figure S20. Capacity contributions from capacitive-controlled and diffusion-controlled reactions of the HC800 electrode at scan rates from 0.2 mV s^{-1} to 1.0 mV s^{-1}.

Text: The cyclic voltammetry method is used to distinguish the plateau capacity region corresponding to diffusion control, while the slope capacity region matches up with the pseudocapacitance control at different scanning rates. The results show that with the increase of scanning rates, the capacitance contribution of the HC800 electrode is higher than that of HC1500-1800 from the scan rate of 0.2 mV s^{-1} to 1.0 mV s^{-1} (**Figure S19, ESI†**). According to the relationship ($i = av^b$) between the peak current (i) and scan rate (v), the b value of 0.5 indicates a diffusion-controlled process, while a b value of 1.0 corresponds to the pseudocapacitance process. Therefore, the HC800 electrode demonstrates a co-controlled process of diffusion and pseudocapacitance with a higher b value, which exhibits factually better kinetic behavior compared to HC1500-180 (**Figure S20, ESI†**).

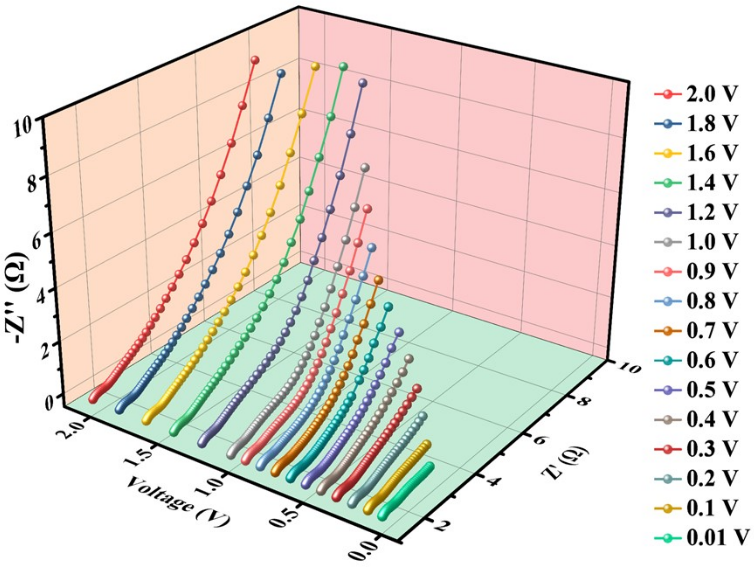

Figure S21. *In-situ* electrochemical impedance spectroscopy (EIS) during the discharging process of HC800.

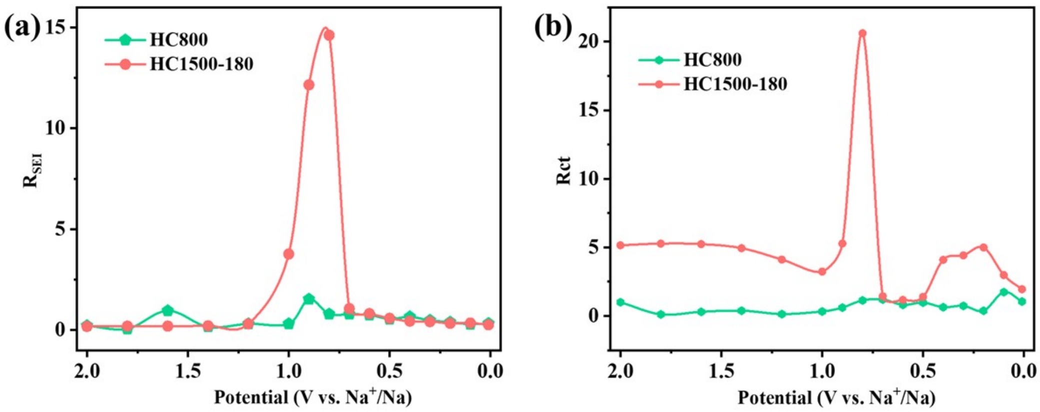

Figure S22. Electrochemical impedance spectroscopy (EIS) curves evolution (a) R_{SEI}, (b) R_{ct} of HC800 and HC1500-180 electrodes at discharging stage from 2.0 V to 0.005 V.

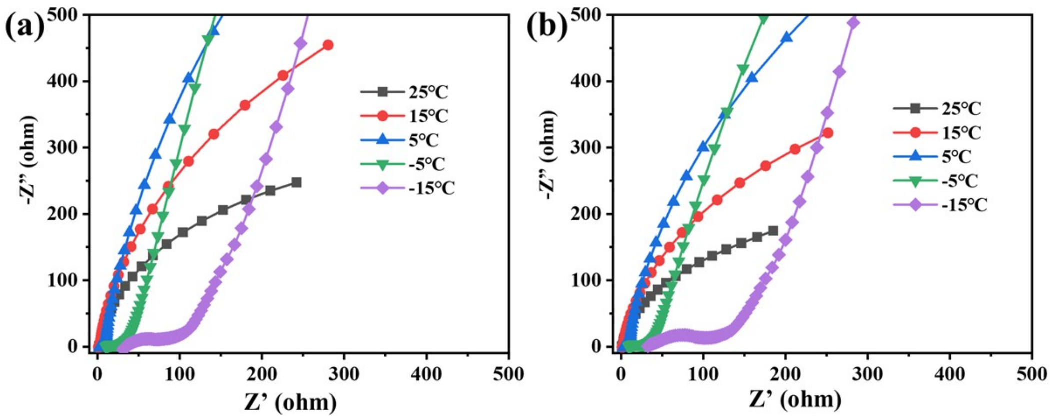

Figure S23. (a-b) Temperature-dependent Nyquist plots of the (a) HC800, and (b) HC1500-180 electrodes.

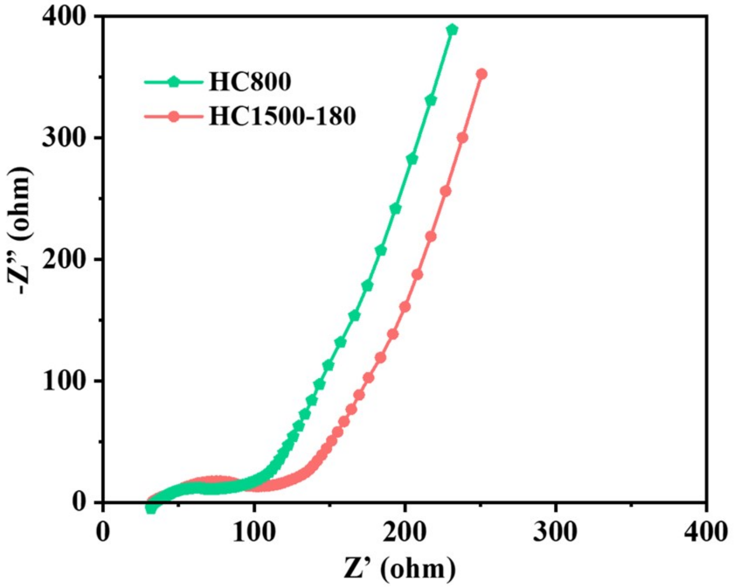

Figure S24. Nyquist plots of the cycled HC800 and HC1500-180 electrodes at a temperature of -15 ℃.

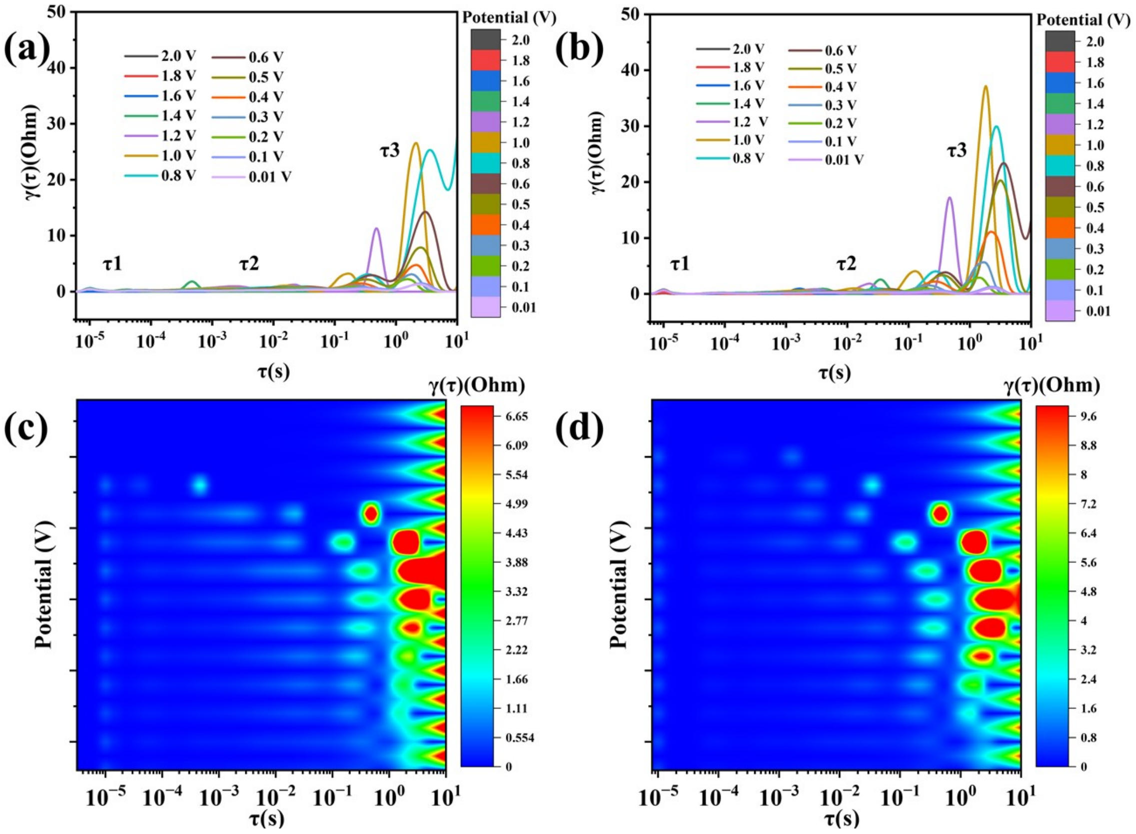

Figure S25. (a-d) Distribution of relaxation times (DRT) plots (τ1, τ2, τ3) obtained by deconvolving the electrochemical impedance spectroscopy (EIS) during the discharging process, the different stages of DRTs (τ1, τ2, τ3) for (a, c) HC800 and (b, d) HC1500-180 electrodes.

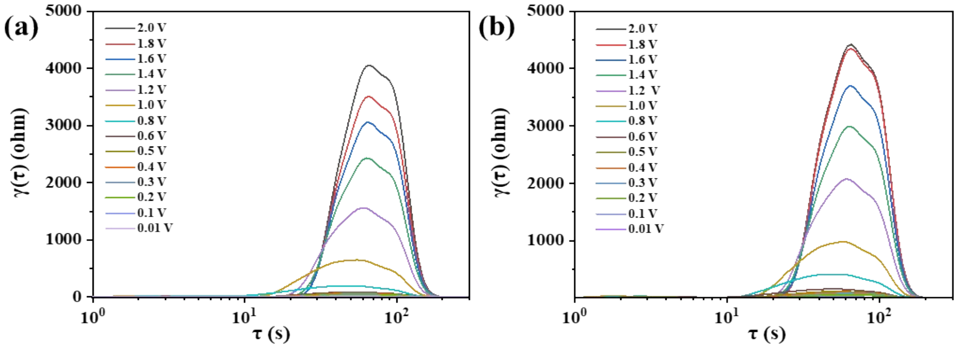

Figure S26. (a-b) Distribution of capacitive times (DCT) plots obtained by deconvolving the electrochemical impedance spectroscopy (EIS) during the discharging process, the different stages of (a) HC800 and (b) HC1500-180 electrode.

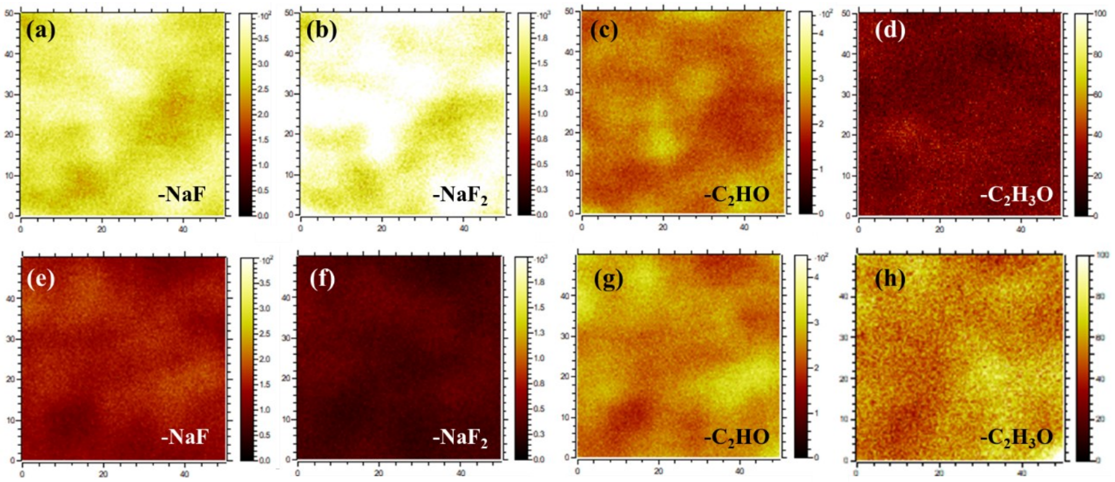

Figure S27. TOF-SIMS secondary ion images of -NaF, $-NaF_2$, $-C_2HO$ and $-C_2H_3O$ fragments after Cs^+ consecutive sputtering for 1800 s for the HC800 and HC1500-180.

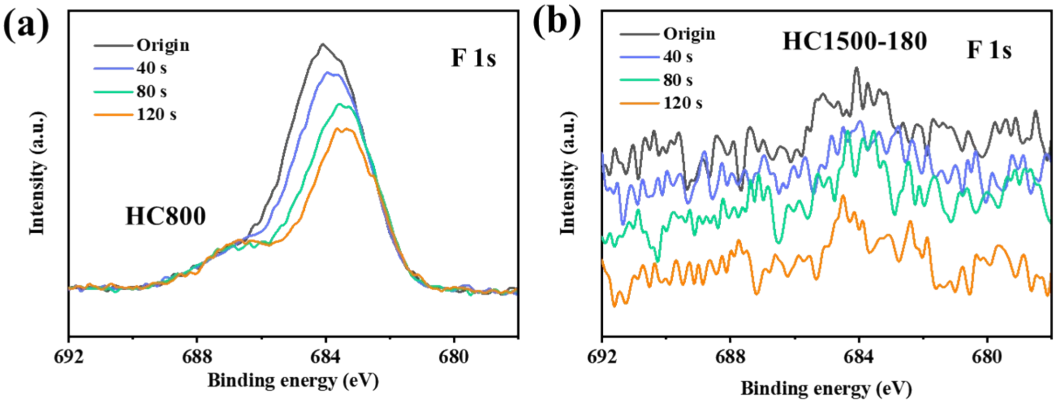

Figure S28. (a-b) Depth-profiling XPS spectra of F 1s of SEI film with different times of argon ion sputtering on HC800 and HC1500-180 electrodes.

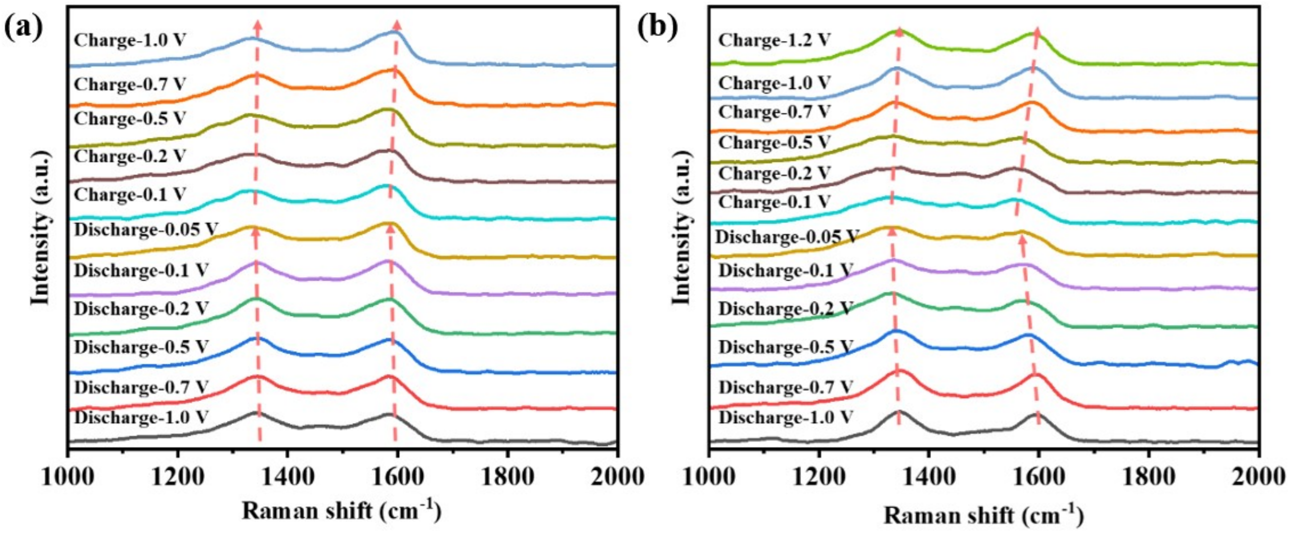

Figure S29. *In-situ* Raman spectra of (a) HC800 and (b) HC1500-180 electrodes during the charge/discharge at a current density of 50 mA g^{-1}.

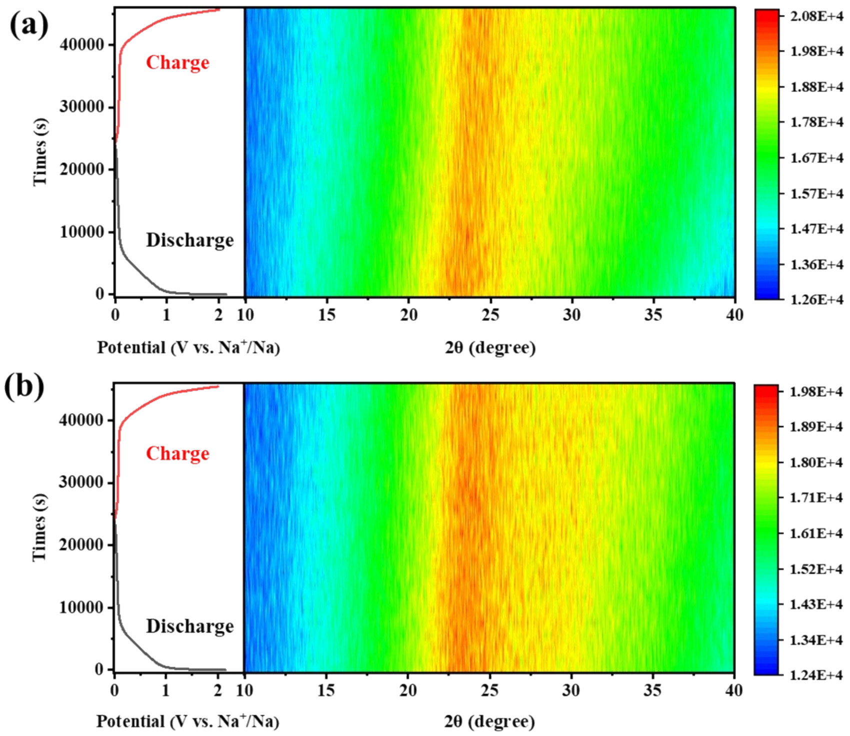

Figure S30. *In-situ* XRD pattern of (a) HC800 and (b) HC1500-180 electrodes during the charge/discharge at a current density of 50 mA g^{-1}.

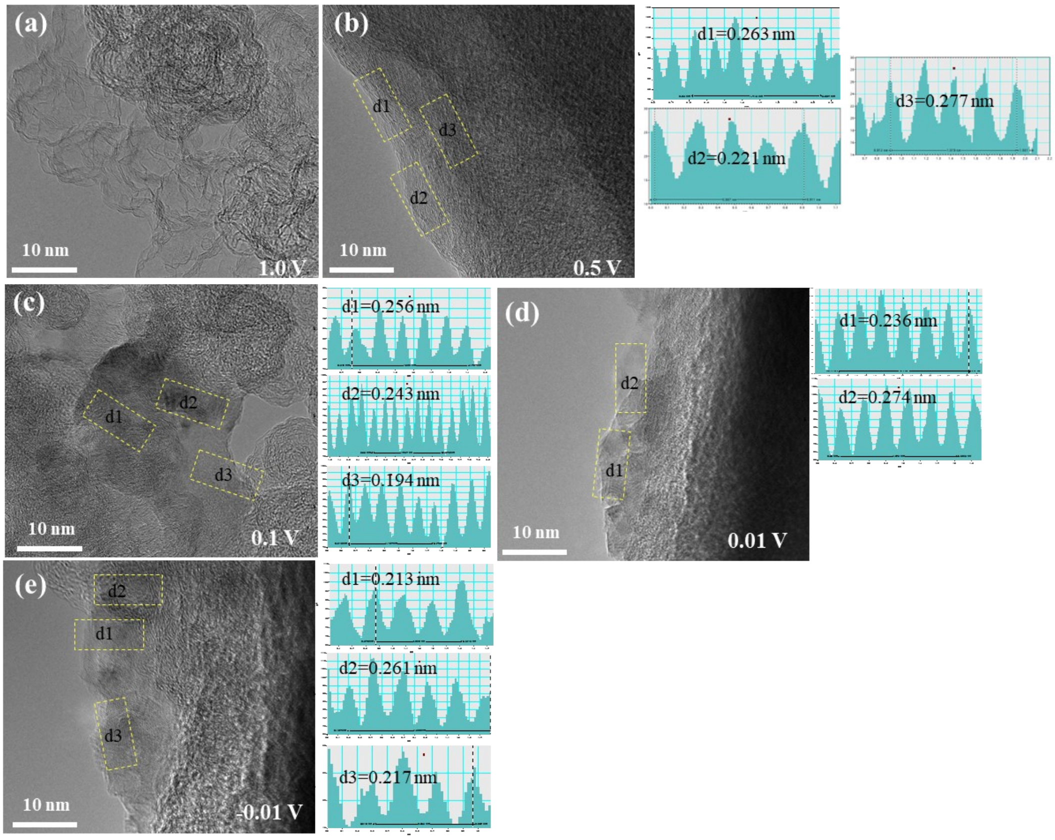

Figure S31. (a-e) ex-TEM images of HC800 electrode at different potentials of the sodiation processes: (a) 1.0, (b) 0.5, (c) 0.1, (d) 0.01, and (e) -0.01 V.

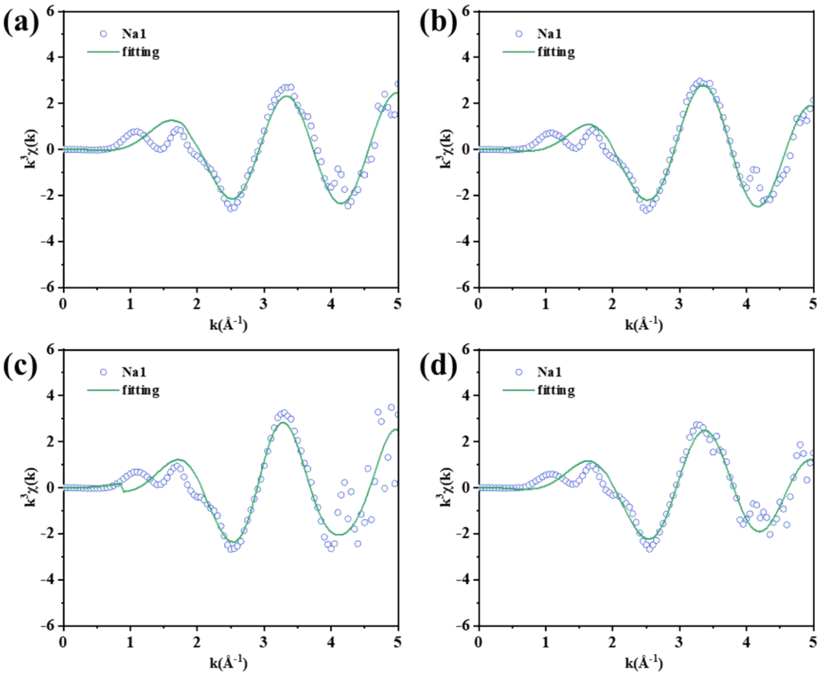

Figure S32. (a-d) ex-situ X-ray absorption spectroscopy of K spaces for HC800 electrode at different potentials of the sodiation processes: (a) 100, (b) 50, (c) 10, and (d) 0 mV.

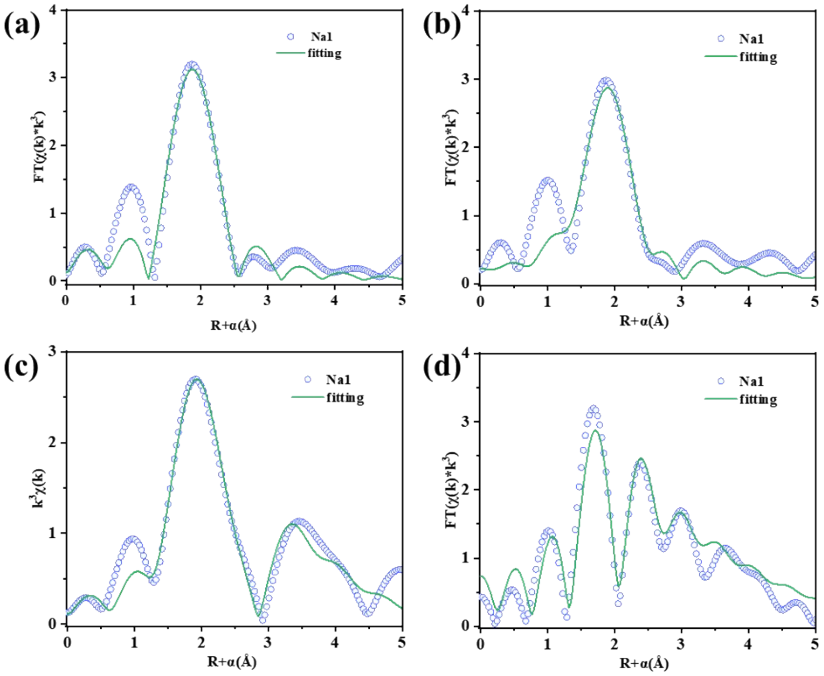

Figure S33. (a-d) ex-situ X-ray absorption spectroscopy of R spaces for HC800 electrode at different potentials of the sodiation processes: (a) 100, (b) 50, (c) 10, and (d) 0 mV.

Table S1. Lattice structure parameters from XRD pattern for the obtained hard carbon samples.

Samples	d_{002} (nm)	L_c (nm)	L_a (nm)
HC500	0.381	0.88	3.70
HC800	0.375	0.99	3.74
HC1100	0.372	1.037	3.76
HC1300	0.369	1.059	3.80
HC1300-180	0.378	1.039	3.35
HC1500-180	0.37	1.079	3.81

Table S2. Graphitization degree from Raman for the obtained hard carbon samples.

Samples	D_1/G	D_2/G	D_3/G
HC500	1.762	0.992	0.987
HC800	1.468	0.955	0.933
HC1100	1.325	0.912	0.912
HC1300	1.315	0.933	0.905
HC1300-180	1.36	0.929	0.937
HC1500-180	1.08	0.937	0.929

Table S3. O1s elements of XPS atomic compositions for the obtained hard carbon samples.

O 1s	C=O (%)	C-O (%)
HC500	72.6	27.4
HC800	61.6	38.4
HC1100	41.9	58.1
HC1300	37.4	62.6
HC1300-180	41.5	58.5
HC1500-180	33.8	66.2

Table S4. Specific surface areas and pore structure by calculated from N_2 adsorption isotherms of the hard carbon.

Samples	Specific surface area/ (m^2 g^{-1})	Average pore size/(nm)	Total pore volume/ (cm^{-3} g^{-1})	Average closed pore size/(nm)
HC500	261	1.89	0.1648	0.6
HC800	4.02	3.57	0.0283	0.62
HC1100	4.86	3.77	0.0351	0.64
HC1300	6.42	1.92	0.0463	0.65
HC1300-180	5.13	5.27	0.0092	0.51
HC1500-180	3.8	4.61	0.009	0.98

Table S5. Different energy cost process of the obtain samples

Samples	Cost1/(kWh)	Cost2/(kWh)	Cost3/(kWh)	Total cost/(kWh)
HC800	-	6.5	2.6	9.1
HC1500-180	-	0	15.6	15.6

Text: To demonstrate the superiority of the strategy we proposed, we roughly calculated the energy cost throughout the process. Take the tube furnace (GSL-1600X with a rated power of 5.2 kW, http://www.kjmti.com/) as an example, the total cost shows the three sections of heating part (cost1, from room temperature to 1500 ℃), keep temperature part (cost2, 800 ℃ with 150 minutes), high temperature insulation part (cost3, 1500 ℃ with different minutes) in **Table S5**. Additionally, since both the traditional strategy and the lattice reconstruction strategy involve the same process of heating from room temperature to 1500 ℃ at the heating rate of 5 ℃/min, keeping the temperature of 1500 ℃ with 300 minutes, which is defined as cost1. Secondly, to highlight the differences, we calculated the energy consumption of different parts of the sintering process. The HC-1500-180 sample maintains the rated power for 180 minutes. So, 5.2 kW (cost3) × 3 h = 15.6 kWh. For the HC800 sample, the 800 ℃ with 150 minutes denotes the 50% rated power, that is 5.2 kW × 50% × 2.5 h (cost2) + 5.2 kW × 0.5 h (cost3) = 9.1 kWh. Therefore, based on the current differences (cost2+cost3), we can find that the lattice reconstruction strategy significantly reduces energy consumption by about 41.67%.

Table S6. EXAFS fitting parameters at the Na K-edge for the HC800.

Stages	Shell	CN	R(Å)	ΔE_0(eV)	R factor
100 mV	Na-O	5.33	2.31	-1.09	0.015
50 mV	Na-O	4.47	2.36	0.848	0.027
10 mV	Na-O	4.28	2.42	2.957	0.026
	Na-Na	8	3.98	2.957	0.026
0 mV	Na-O	5.59	2.35	0.435	0.033
	Na-Na	8	2.98	0.435	0.033

References

[1] F. Wang, L. Chen, J. Wei, C. Diao, F. Li, C. Du, Z. Bai, Y. Zhang, O.I. Malyi, X. Chen, Y. Tang, X. Bao, *Energy Environ. Sci.*, **2025**, 18, 4312-4323.

[2] J. Chen, E. Quattrocchi, F. Ciucci, Y. Chen, *Chem*, **2023**, 9, 2267-2281.

[3] Y. Mo, W. Zhou, K. Wang, K. Xiao, Y. Chen, Z. Wang, P. Tang, P. Xiao, Y. Gong, S. Chen, P. Gao, J. Liu, *ACS Energy Lett.*, **2023**, 8, 995-1002.

[4] M. Schönleber, E. Ivers-Tiffée, *Electrochemistry Communications*, **2015**, 61, 45-48.

[5] P.E. Blöchl, *Physical Review B*, **1994**, 50, 17953-17979.

[6] G. Kresse, J. Hafner, *Physical Review B*, **1993**, 47, 558-561.

[7] G. Kresse, J. Furthmüller, *Computational Materials Science*, **1996**, 6, 15-50.

[8] G. Kresse, J. Furthmüller, *Physical Review B*, **1996**, 54, 11169-11186.

[9] J. Klimeš, D.R. Bowler, A. Michaelides, *Physical Review B*, **2011**, 83, 195131.

[10] G. Mills, H. Jónsson, G.K. Schenter, *Surf. Sci.*, **1995**, 324, 305-337.

[11] H. J Nsson, G. Mills, K.W. Jacobsen, Nudged elastic band method for finding minimum energy paths of transitions, in Classical and Quantum Dynamics in Condensed Phase Simulations, World Scientific, **1998**, 385-404.

[12] M.K. Aydinol, A.F. Kohan, G. Ceder, K. Cho, J. Joannopoulos, *Physical Review B*, **1997**, 56, 1354-1365.

[13] A. Jain, S.P. Ong, G. Hautier, W. Chen, W.D. Richards, S. Dacek, S. Cholia, D. Gunter, D. Skinner, G. Ceder, K.A. Persson, *APL Materials*, **2013**, 1, 011002.

[14] L. Xie, C. Tang, Z. Bi, M. Song, Y. Fan, C. Yan, X. Li, F. Su, Q. Zhang, C. Chen, *Adv. Energy Mater.*, **2021**, 11, 2101650.